Research Square

Preprints are preliminary reports that have not undergone peer review. They should not be considered conclusive, used to inform clinical practice, or referenced by the media as validated information.

Quantum-controlled synthetic materials

Andrei Vrajitoarea

andrei.v@nyu.edu

Department of Physics, Center for Quantum Information Physics, New York University
https://orcid.org/0000-0002-4820-1886

Gabrielle Roberts

University of Chicago https://orcid.org/0000-0003-3309-5205

Kaden Hazzard

Department of Physics and Astronomy, Smalley-Curl Institute, Rice University

Jon Simon

Stanford University https://orcid.org/0000-0001-7854-4647

David Schuster

Stanford University https://orcid.org/0000-0002-0012-3874

Physical Sciences - Article

Keywords:

Posted Date: April 22nd, 2026

DOI: https://doi.org/10.21203/rs.3.rs-9331290/v1

License: This work is licensed under a Creative Commons Attribution 4.0 International License.
Read Full License

Additional Declarations: There is **NO** Competing Interest.

Quantum-controlled synthetic materials

Andrei Vrajitoarea,[1] Gabrielle Roberts,[2] Kaden R. A. Hazzard,[3,4] Jonathan Simon,[5,6] and David I. Schuster[6]

[1] *Center for Quantum Information Physics, Department of Physics, New York University, New York 10003, USA*
[2] *The Department of Physics, The James Franck Institute, and The Pritzker School of Molecular Engineering, The University of Chicago, Chicago, IL*
[3] *Department of Physics and Astronomy, Rice University, Houston, TX, USA*
[4] *Smalley-Curl Institute, Rice University, Houston, TX 77005, USA*
[5] *The Department of Physics, Stanford University, Stanford, CA*
[6] *The Department of Applied Physics, Stanford University, Stanford, CA*

(Dated: April 6, 2026)

Analog quantum simulators and digital quantum computers are two distinct paradigms driving near-term applications in modern quantum science, from probing many-body phenomena to identifying computational advantage over classical systems. A transformative opportunity on the horizon is merging the high-fidelity many-body evolution in analog simulators with the robust control and measurement of digital machines. Such a hybrid platform would unlock new capabilities in state preparation, characterization and dynamical control. Here, we embed digital quantum control in the analog evolution of a synthetic quantum material by entangling the lattice potential landscape of a Bose-Hubbard circuit with an ancilla qubit. This Hamiltonian-level control induces dynamics under a superposition of different lattice configurations and guides the many-body system to novel strongly-correlated states where different phases of matter coexist – ordering photons into superpositions of solid and fluid eigenstates. Leveraging hybrid control modalities, we adiabatically introduce disorder to localize the photons into an entangled cat state and enhance its coherence using a many-body echo technique. This work illustrates the potential for entangling quantum computers with quantum matter – synthetic and solid-state – for advantage in sensing and materials characterization.

I. INTRODUCTION

Advances in programmable quantum simulation platforms have enabled the rapid development of synthetic matter assembled from individual quantized systems with tailored interactions between them. Such platforms offer unique possibilities for exploring many-body physics in a highly controllable way [1–6], by leveraging microscopic and dynamical probes [7, 8] and navigating extreme parameter regimes [9–11] beyond those accessible in solid-state materials. Investigating and utilizing the complex coherent dynamics in these designer many-body systems has broad implications across quantum science, from understanding fundamental phenomena [12], to engineering quantum information processors robust to errors [13, 14] and benchmarking state-of-the-art computational tools [15–17].

Recent efforts in the precise manipulation of isolated programmable many-body systems have shed light on various out-of-equilibrium phenomena, including information scrambling [18, 19] and thermalization [20–22], formation and scaling of entanglement [23, 24], time crystallinity [25, 26], many-body localization [27–30], quantum scarring [31, 32] and anomalous transport [11, 33–35]. Investigating the late-time dynamics in these analog quantum simulators offers a first practical advantage, where moderately-sized quantum systems already challenge state-of-the-art numerical methods [16, 17, 22, 36]. Controlling the many-body dynamics in such programmable systems can also enable other practical applications from generating large-scale entangled states as highly-sensitive metrological probes [37, 38], to solving optimization problems encoded in spin models [39, 40].

While these synthetic materials are fundamentally quantum mechanical, *all* current techniques guide their dynamics through *classical* control of the system Hamiltonian, because the Hamiltonian parameters that dictate the unitary evolution are defined with external, *classical* fields. In analogy to a transistor, where carrier transport across its channel is controlled by a gate voltage, transport dynamics across the system is configured with classical control signals: lattices of (classical) laser beams confine and manipulate atomic simulators; (classical) currents generate the magnetic fields that tune the frequencies of transmons. Can we envision realizing a *quantum-controlled transistor*, such that the evolution of a synthetic many-body system is controlled by *another* quantum system? This capability would open the door to hybrid devices interfacing digital quantum computers with analog simulators and sensors [16].

Controlling & entangling quantum matter with small quantum computers would enable novel protocols for preparing and probing strongly correlated states of matter and light, and new routes to quantum advantage [41–43]. Similar ideas are under active exploration in subwavelength atomic arrays, where the state of a single ancilla atom controls the macroscopic scattering response of an array [44], providing a quantum optical metasurface that can generate highly correlated light such as Greenberger–Horne–Zeilinger and multidimensional cluster states [45]. Furthermore, entangling ancilla qubits with initial states can leverage ancilla-conditioned dynamics to probe anyon braiding phases [46], excitation

spectra [29, 47, 48], and information scrambling [18, 19].

In this work, we demonstrate a quantum-controlled synthetic material in a Bose-Hubbard circuit of strongly interacting microwave photons confined to a lattice of coupled superconducting qubits. Our approach marries the robust site-resolved control of the lattice potential with the qubit control of each individual site to realize Hamiltonian-level quantum control of our many-body system by entangling the lattice energy landscape with an ancilla qubit. Such control enables the system to evolve under a superposition of lattice configurations entangled with the state of the ancilla qubit, thus realizing a photonic transistor where quantum logic is embedded in the analog dynamics of a many-body system. The interfering trajectories guide the system to a first-of-its-kind quantum state where different phases of matter coexist, ordering the photons into a superposition of a solid (Mott insulator [49]) and fluid eigenstate [50] entangled with the ancilla. Following the preparation of this unconventional state, adiabatic site-resolved control of disorder re-localizes the photons to a highly-entangled N00N (cat) state. By entangling the lattice geometry with the state of an ancilla qubit, we can perform Ramsey measurements [48] on the ancilla to learn about the impact of the lattice geometry on the many-body states. Leveraging the hybrid analog-digital control, we introduce a many-body echo protocol to enhance the coherence of the entangled states by decoupling their evolution from low-frequency phase noise.

In what follows, we introduce our circuit platform and the ancilla-conditioned evolution protocol. We apply this protocol to assemble solid + fluid superpositions and their corresponding cat states, employing complementary schemes that utilize the precise control of the lattice potential and fluid excitations. Finally, we employ many-body Ramsey interferometry to probe the coherence of our long-range correlated cat states, and an echo protocol to suppress slow dephasing of the many-body states.

II. QUANTUM CIRCUIT PLATFORM

Our experiments take place in the platform shown in Fig. 1b). The dynamics of this circuit is captured by a 1D Bose-Hubbard model (Fig. 1a)

$$\mathrm{H_{BH}}/\hbar = J\sum_{\langle i,j\rangle} a_i^\dagger a_j + \frac{U}{2}\sum_i n_i\left(n_i-1\right) + \sum_i \left[\omega_0+\delta_i(t)\right]n_i,$$

describing the coherent propagation of bosonic particles (photons) in a lattice, with a nearest-neighbor tunneling rate J, experiencing strong local interactions with an on-site energy U. The operator $a_i^\dagger$ (a_i) creates (destroys) a microwave photon on site i, where the energy of the first photon is $\omega_0+\delta_i$, and $\hbar$ is the reduced Planck's constant.

In our superconducting circuit platform [5, 50, 51]

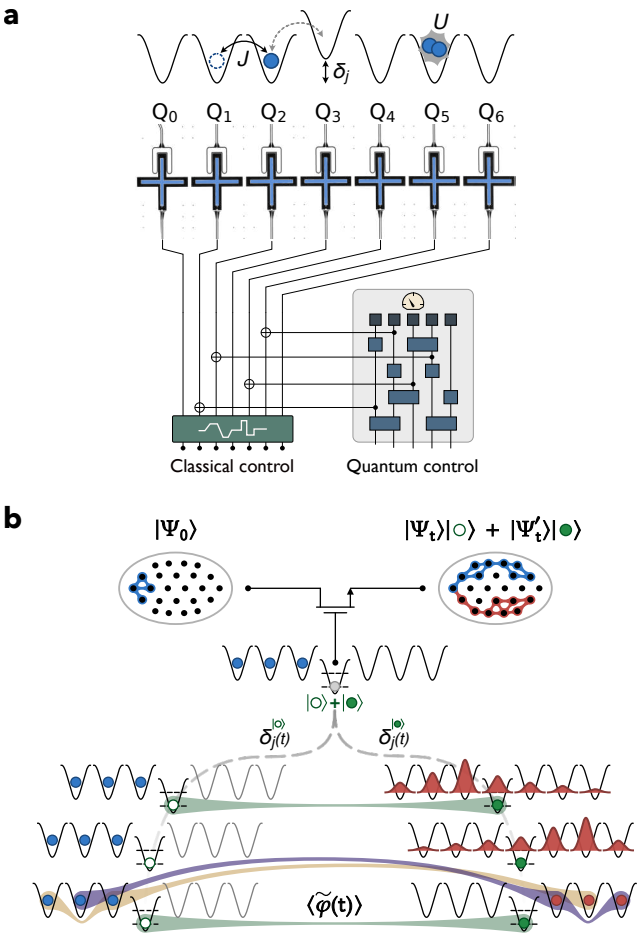

FIG. 1. **Quantum control of transport in a Bose-Hubbard circuit**. **a.** The physical platform used to investigate transport dynamics maps to a 1D Bose-Hubbard model where bosonic particles coherently propagate in a tight-binding lattice and experience strong local interactions. This system is implemented as a chain of capacitively coupled superconducting transmon qubits (blue), serving as the lattice sites that host photonic particles (microwave excitations of the qubits). Inter-site capacitive coupling mediates particle tunneling (J), and the transmon anharmonicity provides local interactions (U). Site-resolved control of the lattice potential landscape is achieved by tuning the transmon resonance energies using inductively coupled bias lines to thread magnetic flux through their SQUID loops. Leveraging the quantum nature of the lattice sites, specifically their occupancy-dependent energy transition, offers a unique capability for steering the entanglement dynamics in our many-body system, by marrying the state preparation protocol of correlated fluids [50] with the quantum control of the lattice energy landscape. **b.** Schematic representation of a quantum-controlled photonic transistor, where the many-body dynamics is regulated by the state of a control site. A superposition of zero and one particles in the control site drives interference between different lattice configurations to generate entangled states with long-range correlations, which we characterize by extracting the phase information of the control qubit.

the tight-binding lattice sites are implemented as transmon qubits [52], the bosonic particles are the qubit's microwave excitations, the tunneling (J) is achieved through the capacitive coupling of neighboring qubits, and the on-site interactions (U) stem from the transmon anharmonicity. The lattice energy landscape is dynamically controlled with site-resolved precision by individually tuning the transmon frequencies using flux bias lines (see SI C). We operate the device with the static parameters $J/2\pi = -9$ MHz, $U/2\pi = -240$ MHz, and a qubit tuning range $(\omega_0 + \delta_i)/2\pi \in [3, 6]$ GHz where we investigate the lattice dynamics at $\omega_0/2\pi \approx 5.31$ GHz. The photon lifetime $T_1 \approx 45\,\mu$s allows many-body effects to dominate over dissipation $|U| \gg |J| \gg 1/T_1$. Each transmon is capacitively coupled to an off-resonant coplanar waveguide resonator to allow site-resolved microscopy of the photon occupation (see SI A).

Capitalizing on the site-resolved control of the lattice potential profile has played a pivotal role in preparing and characterizing many-body states in our synthetic platform. We have harnessed the adiabatic control of lattice disorder ($\delta_i \gg J$) to prepare fluids of light [50], and subsequently engineered lattice perturbations ($\delta_i \approx J$) in real-time ($t \ll J^{-1}$) to probe many-body dynamics [53]. These techniques have thus far relied entirely on classical control of the lattice. We exploit the quantum nature of the actual lattice sites (the transmon qubits), where their transition energy depends upon their occupancy, to create lattice energy landscapes that depend upon the occupancy of several sites. When incorporating state-dependent potentials with superpositions of these occupancies, the system undergoes evolution under a superposition of different lattice configurations, allowing for unconventional control of the many-body dynamics.

This capability becomes the enabling ingredient for implementing a quantum-controlled photonic transistor using ancilla-conditioned lattice potentials (Fig. 1c). The protocol relies on frequency detuning a lattice site by its interaction energy U, to mediate the transport of particles through its doubly-excited state. This resonant tunneling process is allowed *only* if the lattice site is occupied with a photon, thereby making the entire dynamics of the many-body system conditioned on the quantum state of the lattice (control) site. This transistor protocol relies on injecting a superposition of zero and one particles into the control site, enabling the coherent interference of evolution trajectories across different spatial sectors of the lattice. Introducing disorder enables us to controllably freeze the dynamics and prepare a many-body entangled state, with long-range correlations, which we efficiently characterize through Ramsey interferometry of the control qubit.

III. ENTANGLEMENT PROTOCOL

The conditional transport protocol is presented in Fig. 2a. First, we prepare the lattice in the highest energy three-particle state: the imposed disorder localizes *all* many-body eigenstates, enabling us to prepare this state by injecting individual photons into the three sites on the left half of the lattice (Q_0, Q_1, Q_2), via site-resolved microwave π pulses. Additionally, a central ancilla transmon (Q_3) serves as the quantum switch prepared in an arbitrary single-particle state $|\varphi\rangle$. In this disordered lattice configuration, the many-particle eigenstate corresponds to a localized product state $|\Psi_i\rangle = |111\rangle|\varphi\rangle|000\rangle$. We then adiabatically remove the disorder to a quantum-controlled transport configuration, where the middle site is detuned by U and the evolution of the initial product state depends upon the occupancy of this middle site/ancilla qubit. If the ancilla qubit is empty $|\varphi\rangle = |0\rangle$, the particles remain in a localized state corresponding to a Mott insulator of the disorder-free system [49], with a Mott insulator-vacuum domain wall at the center. If the ancilla qubit is excited with a photon $|\varphi\rangle = |1\rangle$, then its (now resonant) doubly excited state allows for tunneling into the other half of the lattice, resulting in a correlated fluid [50]. The measured density profiles for these two distinct ancilla-controlled states are highlighted in the inset of Fig. 2a. The central result of this protocol is the production of a superposition of solid + fluid many-body states through the manipulation of the ancilla: preparing the ancilla qubit in a particle + hole superposition $|\varphi\rangle = \frac{|0\rangle+|1\rangle}{\sqrt{2}}$ using a $\frac{\pi}{2}$ pulse. The final step is to relocalize the photons by adiabatically re-introducing disorder to an inverted configuration where the highest energy three-particle state corresponds to the right half qubits (Q_4, Q_5, Q_6). The conditional many-body evolution maps the solid + fluid state of the disorder-free system to a highly-entangled N00N state $\frac{1}{\sqrt{2}}(|L\rangle + |R\rangle)$ of the disordered system. In this shorthand notation, the N00N (Schrödinger cat) state corresponds to a superposition of having photons on the left half of the lattice (with an empty ancilla) $|L\rangle = |111\rangle|0\rangle|000\rangle$ and having photons on the right half of the lattice (with an excited ancilla) $|R\rangle = |000\rangle|1\rangle|111\rangle$.

The coherence of this long-range correlated state is characterized through the many-body Ramsey interferometry protocol [51] illustrated in Fig. 2b. Following the preparation of the entangled cat state, the system coherently evolves for a hold time Δt to allow the left and right localized states to accumulate a relative phase $\frac{1}{\sqrt{2}}\left(|L\rangle + e^{i\Delta\phi}|R\rangle\right)$ proportional to the energy difference between the two entangled configurations $\Delta\phi = (\omega_R - \omega_L)\Delta t$. Finally, the reversed transport sequence is applied to disentangle the qubits and relocalize the information back into the ancilla qubit $|111\rangle \otimes \frac{1}{\sqrt{2}}\left(|0\rangle + e^{i\Delta\phi}|1\rangle\right) \otimes |000\rangle$. The accrued phase is now entirely encoded in the ancilla qubit, which we can extract through a subsequent $\frac{\pi}{2}$ pulse followed by a single-qubit measurement in the occupation basis $|0\rangle, |1\rangle$. Plotting the ancilla occupation versus the hold time yields the sinusoidal Ramsey fringes shown in Fig. 2c. These measured oscillations have a contrast limited by

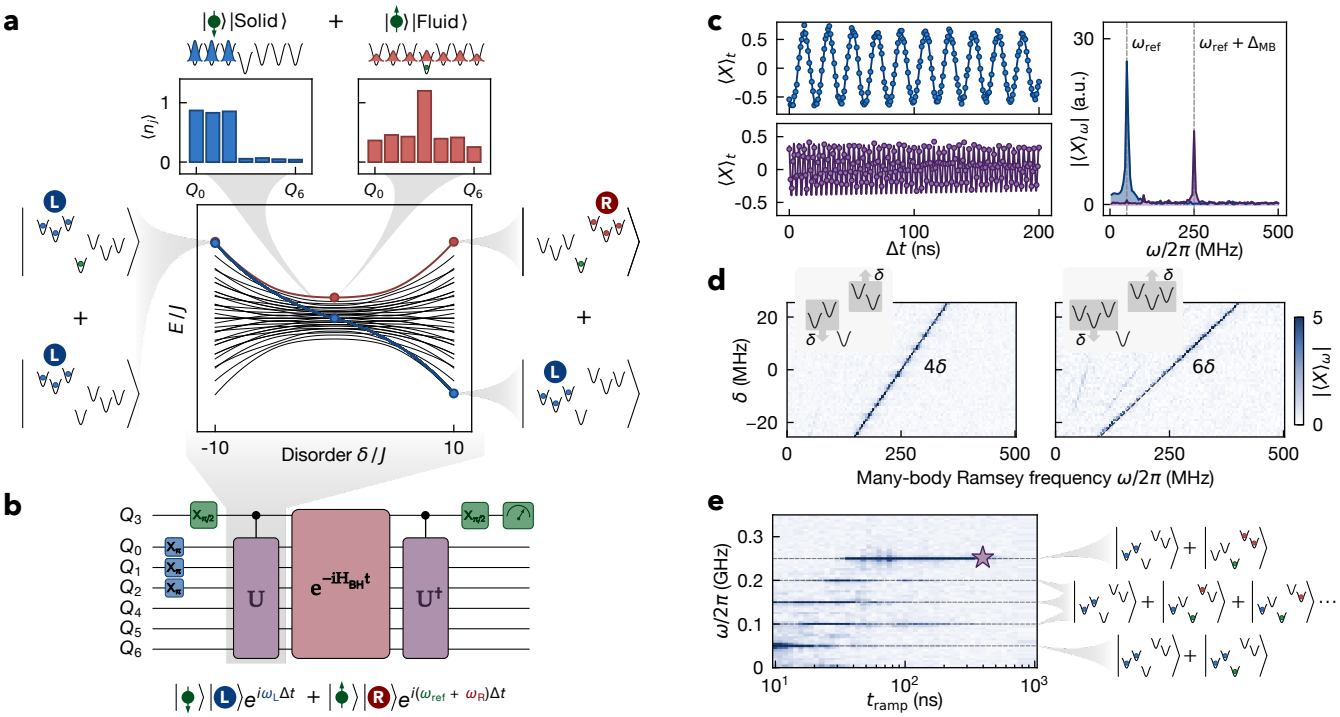

FIG. 2. **Many-body entangling operation via ancilla-conditioned transport**. **a.** Starting in a highly disordered configuration (computational basis), we initialize the highest energy state by exciting the qubits on the left-hand side, and adiabatically remove disorder to a quantum-controlled transport configuration, where the middle site is detuned by U and mediates dynamics between the two halves of the system through its doublon state. If this ancilla qubit is in its ground (excited) state, the particles localize (delocalize) into a solid (fluid), as shown by the measured density profile in blue (red). Preparing the ancilla in a particle + hole superposition ($\frac{\pi}{2}$ pulse) produces a solid + fluid superposition, which maps to a many-body entangled (N00N) state in the computational basis when we adiabatically relocalize the photons to an inverted disordered configuration. **b.** The coherence of such entangled states is probed through many-body Ramsey interferometry: we coherently evolve the entangled state for a time Δt to accumulate a relative phase proportional to the energy difference of the left and right qubit clusters, and apply the corresponding disentangling operation to relocalize the phase information into the ancilla qubit accessible from its population measurement following a second $\frac{\pi}{2}$ pulse. **c.** The frequency difference in the ancilla interference fringe when it is uncoupled (blue) and entangled (purple) with the lattice matches the energy difference between the left and right qubit clusters $\omega_L - \omega_R$, consistent with the preparation of the coherent cat-like superposition of these two collective states. **d.** To leverage this N00N state, we benchmark our system's capability as a sensor: we offset the energy of the right/left qubit clusters by $\pm\delta$ during the phase evolution and observe an increased sensitivity, where the shift in the many-body Ramsey frequency scales with system size $(N-1)\delta$ for both $N = 5$ (left) & $N = 7$ (right) qubit N00N states. **e.** Adiabaticity is characterized by varying the ramp time t_{ramp}, where discrete changes in the Ramsey Fourier frequencies reveal the transition from a product to a fully entangled state.

qubit dephasing (see SI A), and a frequency that is down-converted from the ancilla's natural precession frequency through a Δt-dependent phase offset on the second $\frac{\pi}{2}$ pulse (see SI B). The fringe frequency becomes the defining feature for validating entanglement: the frequency difference in the measured fringes when the ancilla qubit is uncoupled (no photons injected in the lattice) and entangled (transport protocol) with the lattice is equal to the energy difference between the left and right qubit clusters in the disordered configuration. The validation is twofold: the oscillations demonstrate a coherent superposition of multi-qubit eigenstates and the measured fringe frequency is consistent with the preparation of an entangled N00N state.

We further validate the structure of multipartite entanglement in our synthetic material by benchmarking it as a *sensor*, in this case for measuring an energy imbalance between sites to the left and right of our quantum-controlled switch. We demonstrate this principle by introducing external perturbations to the lattice during the Ramsey evolution Δt: the sites on the right (left) side of the ancilla are frequency shifted by a small offset $+(-)\delta$. For uncorrelated lattice site occupations, this energy shift can be directly detected from individual Ramsey measurements on each qubit picking up the relative phase $\Delta\phi = \delta\Delta t$ in the measured fringe frequency. Leveraging our entanglement preparation technique combined with the single-qubit Ramsey probe, we achieve an improved sensitivity from the collective enhancement of the acquired phase $\Delta\phi = (N-1)\delta\Delta t$ leading to an increased

fringe frequency. The $N-1$ prefactor appears instead of N because the ancilla frequency is deliberately kept constant during the perturbed Ramsey sequence. This measurement is conducted for $N=5$ and $N=7$ qubits, as shown in Fig. 2d. The results clearly highlight the collective shift $(N-1)\delta$ of the many-body Ramsey fringe frequency in response to the applied lattice perturbation, serving as a definitive signature of assembling the entangled N00N state.

The entanglement generation protocol relies on the ability to adiabatically assemble and disassemble the solid + fluid many-body superposition. Similar to the adiabatic preparation of correlated fluids [50, 54, 55], this becomes a balancing act between evolving the system at a slow enough rate (relative to the energy gaps) to satisfy adiabaticity, and a fast enough rate to avoid particle loss/dephasing (set by the photon T_1/T_2 lifetimes). We identify this optimum ramp rate by monitoring the Fourier spectrum of the ancilla Ramsey fringes as a function of the ramp duration t_{ramp}. We perform this measurement for an $N=5$ site lattice as shown in Fig. 2e, where the ramp time is varied over two orders of magnitude. For very fast ramps $t_{\mathrm{ramp}} \ll J^{-1}$, the photons remain localized as they lack time to move at all, even when the transport is otherwise unimpeded. In this scenario, the ancilla is uncoupled from the other sites and is precessing at its reference frequency $\omega_{\mathrm{ref}}/2\pi \simeq 50\,\mathrm{MHz}$ which coincides with the dominant frequency component in the measured Ramsey fringe. For intermediate ramps $t_{\mathrm{ramp}} \approx J^{-1}$, the photons do not adiabatically follow the conditioned trajectories in Fig. 2a, but diabatically delocalize to other fluid eigenstates. These diabatic excitations in the ordered lattice are mapped to W-like entangled states in the disordered configuration, appearing as discrete frequency components in the Ramsey spectrum. Further increasing the ramp time $t_{\mathrm{ramp}} \gg J^{-1}$ ensures the photons adiabatically delocalize into the target fluid state and conditionally prepares the solid + fluid many-body state. This progression from a product state to the final entangled state is captured as a single frequency component prevailing in the measured Ramsey spectrum, corresponding to the fringe frequency $(\omega_{\mathrm{ref}}+\omega_R-\omega_L)/2\pi \simeq -250\,\mathrm{MHz}$ for the N00N state. The measured signal is folded about the 500 MHz Nyquist limit and thus appears as a frequency component at 250 MHz. Evolving for longer ramp times, decoherence effects manifest as a decreased Ramsey fringe contrast and thus a diminished peak amplitude of the Fourier component associated with the entangled state.

IV. CONDITIONAL PHONON TRANSPORT

A complementary approach for creating cat states is inspired by the observation that they can be constructed through a conditional multi-qubit SWAP operation: photons from the left half of the lattice are transferred over the right half only if the middle ancilla qubit is excited.

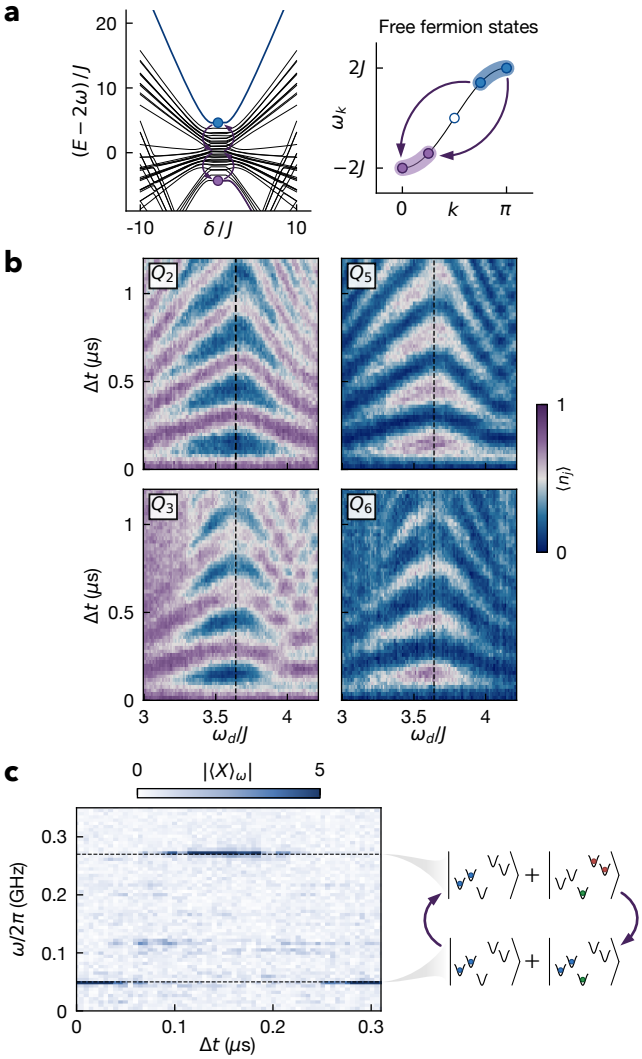

FIG. 3. **Phonon-assisted SWAP operation**. **a.** Entanglement generation using conditional phonon dynamics is demonstrated for $N=5$ qubits. Phonons are excited in the adiabatically prepared fluid through the potential modulation of a single lattice site (flux driving the transmon), creating a particle-hole excitation. Driving the lattice site at $\omega_d \approx 3.6J$ induces a two-phonon process that inverts the population of the free fermion eigenstates (diagram). **b.** Adiabatically reintroducing disorder turns the phonon creation process into a many-body SWAP operation in the computational basis, where the highest frequency qubits (Q_2, Q_3) simultaneously exchange photons with the lowest frequency qubits (Q_5, Q_6). In contrast, this lattice perturbation does not affect the solid (Mott insulator) eigenstate, since it is incompressible ($\omega_d \ll U$). Therefore, applying this phonon drive to the $|\mathrm{solid}\rangle + |\mathrm{fluid}\rangle$ phase leads to a similar swap operation conditioned on the state of the ancilla (Q_4). **c.** The preparation of the target entangled state is clearly captured in a many-body Rabi experiment: the ancilla Ramsey frequency is probed as a function of the phonon drive duration, and we observe a cyclic transition from the product state to the entangled cat state.

We demonstrate this protocol for a $N = 5$ site lattice in Fig. 3. The SWAP operation itself leverages the one-to-one correspondence between the product states in the disordered system and the fluid eigenstates in the disorder-free transistor configuration, where photons localized on the left (Q_2, Q_3) and right (Q_5, Q_6) sides of the disordered lattice are adiabatically connected to the highest and lowest energy fluid eigenstates in the two-particle hard-core band, respectively. The intuition gained from mapping fluid states of hardcore bosons to free fermions [56], as shown in Fig. 3a, reveals that such few-body SWAP operations are equivalent to inverting the population of occupied & empty free-fermion eigenstates. This population transfer is enabled by creating particle-hole excitations – specifically *phonons* – corresponding to collective modes in the fluid. These phonon excitations are generated by perturbing the lattice potential, by modulating the energy of a single lattice site $\varepsilon_d \cos(\omega_d t) n_i$ (through flux driving the transmon) with a drive frequency ω_d (see SI E). In practice, we modulate the site Q_3 site at $\omega_d \approx 3.6J$ (with a constant drive amplitude ε_d) to drive a two-phonon transition between the fluid states at the edges of the hard-core band. Adiabatically tuning the qubits back to their initial disordered configuration converts the phonon creation in the fluid basis to a multi-qubit SWAP operation in the computational basis. This process, highlighted in Fig. 3b, simultaneously exchanges photons between the higher (Q_2, Q_3) and lower (Q_5, Q_6) frequnecy sites.

Implementing the ancilla-conditioned SWAP operation follows naturally from applying the phonon drive to our solid + fluid state prepared in the transistor configuration. In contrast to the fluid, the solid (Mott insulating) state is not affected by the lattice modulation since it is an *incompressible* state with an interaction-induced gap larger than the phonon drive frequency ($U \gg \omega_d$). Benchmarking the operation is then simply a matter of monitoring the Q_4 ancilla Ramsey fringe frequency as we vary the duration of the phonon drive, as shown in Fig. 3c. This presents the multi-particle version of a Rabi oscillation, whereby we periodically cycle between the product $|11\rangle\frac{1}{\sqrt{2}}(|0\rangle + |1\rangle)|00\rangle$ and entangled $\frac{1}{\sqrt{2}}(|11\rangle|0\rangle|00\rangle + |00\rangle|1\rangle|11\rangle)$ states. This technique of optimizing single-qubit drive parameters (for inducing phonons) with respect to a single qubit observable (ancilla fringes) highlights the versatility of our platform for implementing few-body entangling operations.

V. MANY-BODY ECHO

While N00N states exhibit greater resilience to correlated phase noise compared to Greenberger-Horne-Zeilinger (GHZ) states [57], they still remain vulnerable to losses and dephasing as the system size grows, causing the scaling of the phase sensitivity to degrade from the Heisenberg limit to the standard quantum limit [58, 59]. In our protocol, the entanglement-enhanced phase accumulation (set by the energy imbalance between the two cat components) is an order of magnitude faster than the photon transport (set by the tunneling rate J). Consequently, the system spends more time adiabatically traversing the many-body eigenstate trajectories (see Fig. 2a) than performing entanglement-enhanced sensing in the N00N state. The fidelity of preparing and probing these entangled states is thus constrained by decoherence during the adiabatic ramps, which, in the case of our flux-tunable transmon sites, is limited by dephasing noise with $T_2 \approx 4\mu s$.

The hybrid nature of our platform – which allows for coupling quantum computers to many-body systems – provides a unique opportunity to exploit control tools to enhance the coherence of many-body states. Specifically, we circumvent the decoherence bottleneck tied to the preparation of our N00N states by employing an echo protocol tailored to dynamically decouple the many-body evolution from low-frequency phase noise, thereby refocusing the ancilla phase information [60]. Echo protocols are also actively investigated for preparing many-body entangled states in Ising spin chains and Rydberg atom arrays [61].

Our many-body echo protocol, displayed in Fig. 4a, represents a generalization of the Ramsey sequence (Fig. 2b). The system evolves in a series of alternating entangling (U_{MB}) and disentangling ($U^\dagger_{\mathrm{MB}}$) transport sequences, inserting a hold time Δt in between the final pair of operations to accumulate the many-body phase information in the ancilla qubit. The key feature of this echo procedure is the application of a π-pulse on the ancilla qubit in the middle of the sequence, akin to a Hahn spin echo [62]. This inversion refocuses the delicate phase information in the ancilla qubit by effectively reversing the accumulated phase error arising from shot-to-shot flux noise during the adiabatic ramps. Applying a single pair of entangling and disentangling operations before and after the ancilla π-rotation is sufficient to dynamically refocus the ancilla phase information and thus enhance its coherence, as demonstrated by the measured Ramsey fringes for the five- and seven-qubit N00N states. While the echo pulse results in noticeably higher contrast oscillations for the five-qubit state, its effect is most pronounced in the seven-qubit state, shown in Fig. 4b, where coherence is undetectable with the standard Ramsey sequence and fringe oscillations emerge only when the echo is applied.

To characterize the performance of the entangling protocol, we quantify the coherence of the prepared N00N state associated with the off-diagonal elements of its density matrix. The coherence is accessible from the amplitude of the measured many-body Ramsey fringes, analogous to probing parity oscillations in GHZ states [57]. Using error amplification, we apply repeated pairs of entangling and disentangling operations to estimate the off-diagonal error of a single entangling operation. The extended echo sequence displayed in Fig. 4a is used for estimating the average off-diagonal error ϵ_X by fit-

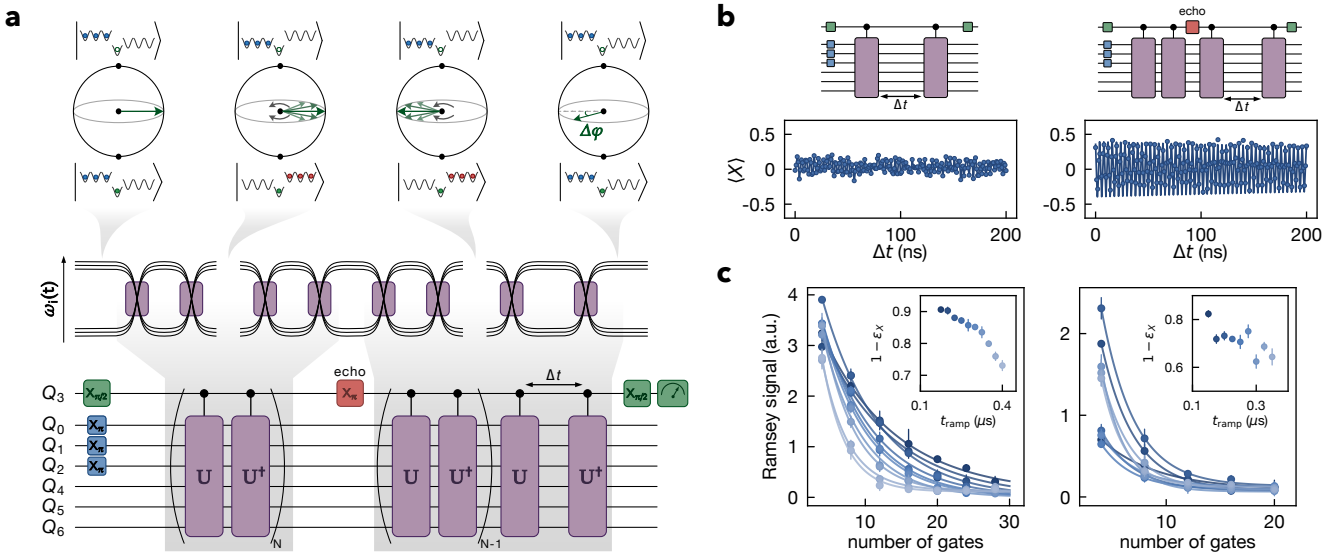

FIG. 4. **Many-body echo**. **a.** An echo protocol is employed to dynamically decouple low-frequency (compared to the evolution time) phase noise during the adiabatic evolution of the entangling operation. The control sequence is an extension of the many-body Ramsey procedure, applying pairs of entangling (U_{MB}) and disentangling ($U_{\mathrm{MB}}^{\dagger}$) operations by adiabatically modulating the qubit-site frequencies $\omega_i(t)$. The many-body phase information $\Delta\phi$ is relocalized in the ancilla qubit by inserting the Ramsey hold time Δt prior to the last disentangling operation. The low-frequency phase noise, accrued during the adiabatic ramps, is averaged out by driving the ancilla with a π-pulse in the middle of the sequence. **b.** Dynamically refocusing the ancilla phase information enhances the measured Ramsey fringes, as demonstrated for the seven-qubit N00N state: a standard Ramsey sequence (left) yields no detectable coherence, whereas an echo sequence (right) yields visible fringe oscillations. **c.** We quantify the fidelity of preparing the off-diagonal elements of the density matrix as a direct measure of coherence. The extended echo sequence is used for amplifying and estimating the off-diagonal error ϵ_X in each entangling/disentangling operation by measuring the decay in the ancilla echo signal (magnitude of the Fourier component) $\langle X\rangle_\omega = A(1-\epsilon_X)^{4N}$. For the five- and seven-qubit N00N states we measure an average error of $\epsilon_X = (9.1 \pm 0.9)\%$ and $(17.7 \pm 1.3)\%$, respectively. Preparation errors further increase as we increase the duration of the adiabatic ramp (inset plots).

ting the decay in the measured ancilla echo signal to $\langle X\rangle_\omega(N) = A(1-\epsilon_X)^{4N}$, where N is the number of entangling-disentangling pair operations applied prior to the echo pulse. As shown in Fig. 4c, we measure an average error rate of $\epsilon_X = (9.1 \pm 0.9)\%$ for the five-qubit N00N state, and $\epsilon_X = (17.7 \pm 1.3)\%$ for the seven-qubit state. Additionally, we estimate the errors associated with the non-adiabatic evolution of our many-body system by probing the fidelity of reversing the entanglement generation. The sequence, detailed in SI D, involves applying multiple pairs of entangling and disentangling operations and measuring the probability of returning the system to its initial product state by probing the final occupation of the lattice sites initially injected with photons. The average reversibility error ϵ_{rev} is obtained from fitting the fidelity metric to $\mathcal{F}_{\mathrm{adb}}(N) = A(1-\epsilon_{\mathrm{rev}})^{2N}$. We extract error rates of $(5.4 \pm 0.2)\%$ and $(4.7 \pm 0.2)\%$ for the five- and seven-qubit entangled states. These errors closely match the values limited by single-qubit decoherence, extracted from decoupling the entangling dynamics by running the same sequence with the ancilla qubit in the ground state.

VI. CONCLUSION AND OUTLOOK

In this work we have explored the consequences of using a minimal quantum computer to control the evolution of a quantum many-body systems To realize this control, we have devised a new protocol that employs ancilla-conditioned dynamics to steer these synthetic many-body systems to unconventional strongly-correlated states where different phases of matter coexist in superposition. Instead of adopting the conventional approach of entangling an ancilla qubit to the initial state [19, 46, 48], we entangle the ancilla to the Hamiltonian degrees of freedom that drive the coherent evolution, as this approach can navigate larger sectors of the Hilbert space. This Hamiltonian-level entanglement with an ancilla qubit further facilitates the efficient extraction of information reflecting the energies of the constituent many-body states, from a Ramsey measurement of the accumulated phase localized in the ancilla qubit.

Our protocol entangles the potential profile of a 1D tight-binding lattice of capacitively coupled transmon qubits, implementing a quantum-controlled transistor where a tunnel-barrier regulating transport of microwave photons along the lattice depends on the state of an ancilla qubit. Injecting photons on one side of the lattice

in a Mott insulating state and setting the ancilla qubit in $\frac{1}{\sqrt{2}}(|0\rangle + |1\rangle)$ allows the entire many-body system to evolve to a $\frac{1}{\sqrt{2}}(|\text{solid}\rangle + |\text{fluid}\rangle)$ state which is subsequently adiabatically mapped to a highly-entangled cat state in the computational basis of the transmon lattice sites. Combining this ancilla-conditioned entangling operation with its time-reversed counterpart into a Ramsey sequence enables the direct measurement of long-range coherence from the ancilla Ramsey fringe. The fringe frequency is proportional to the energy difference between the multi-qubit cat components, acting as a witness for detecting and quantifying the multipartite entanglement in our many-body system using concepts typically employed in metrology [63].

Marrying ancilla-conditioned many-body operations with Ramsey spectroscopy provides a powerful framework for various key applications in quantum science. With a larger control register, such an approach could enhance the sensitivity and dynamic range of many-body sensors by embedding quantum Fourier transforms into the entangling dynamics [64]. Generalizations of our echo-based dynamical decoupling scheme, combined with multi-qubit operations, suggest a new quantum signal processing algorithm [65]. Furthermore, this protocol can be adapted to measure the entanglement spectrum of many-body states from Ramsey spectroscopy of a single control qubit that conditions the global swap between two copies of the state [66]. More broadly, this work demonstrates that integrating analog many-body systems with small quantum computers creates a powerful synergy, offering new avenues for efficiently probing properties of synthetic matter and generating large-scale entanglement in information processors.

VII. ACKNOWLEDGMENTS

This work was supported by ARO MURI Grant W911NF-15-1-0397, AFOSR MURI Grant FA9550-19-1-0399, and by NSF Eager Grant 1926604. Support was also provided by the Chicago MRSEC, which is funded by NSF through Grant DMR-1420709. A.V. acknowledges support from the MRSEC-funded Kadanoff-Rice Postdoctoral Research Fellowship. G.R. acknowledges support from the NSF GRFP. K.R.A.H. acknowledges support from the National Science Foundation (PHY-1848304, DGE-2346014), the Department of Energy (DE-SC0024301), the W. M. Keck Foundation (Grant No. 995764), and the Office of Naval Research (N00014-20-1-2695). We acknowledge support from the Samsung Advanced Institute of Technology Global Research Partnership. Devices were fabricated in the Pritzker Nanofabrication Facility at the University of Chicago, which receives support from Soft and Hybrid Nanotechnology Experimental (SHyNE) Resource (NSF ECCS-1542205), a node of the National Science Foundation's National Nanotechnology Coordinated Infrastructure.

VIII. AUTHOR CONTRIBUTIONS

The experiments were designed by A.V., G.R., J.S., and D.I.S. The collection of data was handled by A.V. Theoretical support was provided by K.H. All authors analyzed the data and contributed to the manuscript.

IX. COMPETING INTERESTS

The authors declare no competing financial or non-financial interests.

[1] Bloch, I., Dalibard, J. & Nascimbene, S. Quantum simulations with ultracold quantum gases. *Nature Physics* **8**, 267–276 (2012).
[2] Blatt, R. & Roos, C. F. Quantum simulations with trapped ions. *Nature Physics* **8**, 277–284 (2012).
[3] Aspuru-Guzik, A. & Walther, P. Photonic quantum simulators. *Nature Physics* **8**, 285–291 (2012).
[4] Browaeys, A. & Lahaye, T. Many-body physics with individually controlled rydberg atoms. *Nature Physics* **16**, 132–142 (2020).
[5] Carusotto, I. *et al.* Photonic materials in circuit quantum electrodynamics. *Nature Physics* **16**, 268–279 (2020).
[6] Monroe, C. *et al.* Programmable quantum simulations of spin systems with trapped ions. *Reviews of Modern Physics* **93**, 025001 (2021).
[7] Bakr, W. S., Gillen, J. I., Peng, A., Fölling, S. & Greiner, M. A quantum gas microscope for detecting single atoms in a hubbard-regime optical lattice. *Nature* **462**, 74–77 (2009).
[8] Cheuk, L. W. *et al.* Quantum-gas microscope for fermionic atoms. *Phys. Rev. Lett.* **114**, 193001 (2015).
[9] Simon, J. *et al.* Quantum simulation of antiferromagnetic spin chains in an optical lattice. *Nature* **472**, 307–312 (2011).
[10] Kollár, A. J., Fitzpatrick, M. & Houck, A. A. Hyperbolic lattices in circuit quantum electrodynamics. *Nature* **571**, 45–50 (2019).
[11] Vrajitoarea, A. *et al.* Ultrastrong light-matter interaction in a multimode photonic crystal. *arXiv preprint arXiv:2209.14972v2* (2024).
[12] Cirac, J. I. & Zoller, P. Goals and opportunities in quantum simulation. *Nature physics* **8**, 264–266 (2012).
[13] Bluvstein, D. *et al.* A quantum processor based on coherent transport of entangled atom arrays. *Nature* **604**,

451–456 (2022).
[14] Acharya, R. *et al.* Quantum error correction below the surface code threshold. *Nature* **638**, 920–926 (2025).
[15] Eisert, J., Friesdorf, M. & Gogolin, C. Quantum many-body systems out of equilibrium. *Nature Physics* **11**, 124–130 (2015).
[16] Daley, A. J. *et al.* Practical quantum advantage in quantum simulation. *Nature* **607**, 667–676 (2022).
[17] Trivedi, R., Franco Rubio, A. & Cirac, J. I. Quantum advantage and stability to errors in analogue quantum simulators. *Nature Communications* **15**, 6507 (2024).
[18] Landsman, K. A. *et al.* Verified quantum information scrambling. *Nature* **567**, 61–65 (2019).
[19] Mi, X. *et al.* Information scrambling in quantum circuits. *Science* **374**, 1479–1483 (2021).
[20] Rigol, M., Dunjko, V. & Olshanii, M. Thermalization and its mechanism for generic isolated quantum systems. *Nature* **452**, 854–858 (2008).
[21] Kaufman, A. M. *et al.* Quantum thermalization through entanglement in an isolated many-body system. *Science* **353**, 794–800 (2016).
[22] Andersen, T. I. *et al.* Thermalization and criticality on an analogue–digital quantum simulator. *Nature* **638**, 79–85 (2025).
[23] Joshi, M. K. *et al.* Exploring large-scale entanglement in quantum simulation. *Nature* **624**, 539–544 (2023).
[24] Karamlou, A. H. *et al.* Probing entanglement in a 2d hard-core bose–hubbard lattice. *Nature* **629**, 561–566 (2024).
[25] Zhang, J. *et al.* Observation of a discrete time crystal. *Nature* **543**, 217–220 (2017).
[26] Choi, S. *et al.* Observation of discrete time-crystalline order in a disordered dipolar many-body system. *Nature* **543**, 221–225 (2017).
[27] Schreiber, M. *et al.* Observation of many-body localization of interacting fermions in a quasirandom optical lattice. *Science* **349**, 842–845 (2015).
[28] Choi, J.-y. *et al.* Exploring the many-body localization transition in two dimensions. *Science* **352**, 1547–1552 (2016).
[29] Roushan, P. *et al.* Spectroscopic signatures of localization with interacting photons in superconducting qubits. *Science* **358**, 1175–1179 (2017).
[30] Guo, Q. *et al.* Observation of energy-resolved many-body localization. *Nature Physics* **17**, 234–239 (2021).
[31] Bernien, H. *et al.* Probing many-body dynamics on a 51-atom quantum simulator. *Nature* **551**, 579–584 (2017).
[32] Bluvstein, D. *et al.* Controlling quantum many-body dynamics in driven rydberg atom arrays. *Science* **371**, 1355–1359 (2021).
[33] Brown, P. T. *et al.* Bad metallic transport in a cold atom fermi-hubbard system. *Science* **363**, 379–382 (2019).
[34] Joshi, M. K. *et al.* Observing emergent hydrodynamics in a long-range quantum magnet. *Science* **376**, 720–724 (2022).
[35] Belyansky, R. *et al.* Frustration-induced anomalous transport and strong photon decay in waveguide qed. *Phys. Rev. Res.* **3**, L032058 (2021).
[36] Haghshenas, R. *et al.* Digital quantum magnetism at the frontier of classical simulations. *arXiv preprint arXiv:2503.20870* (2025).
[37] Degen, C. L., Reinhard, F. & Cappellaro, P. Quantum sensing. *Rev. Mod. Phys.* **89**, 035002 (2017).
[38] Ye, J. & Zoller, P. Essay: Quantum sensing with atomic, molecular, and optical platforms for fundamental physics. *Phys. Rev. Lett.* **132**, 190001 (2024).
[39] Cerezo, M. *et al.* Variational quantum algorithms. *Nature Reviews Physics* **3**, 625–644 (2021).
[40] Bharti, K. *et al.* Noisy intermediate-scale quantum algorithms. *Rev. Mod. Phys.* **94**, 015004 (2022).
[41] Gilyén, A., Su, Y., Low, G. H. & Wiebe, N. Quantum singular value transformation and beyond: exponential improvements for quantum matrix arithmetics. In *Proceedings of the 51st annual ACM SIGACT symposium on theory of computing*, 193–204 (2019).
[42] Martyn, J. M., Rossi, Z. M., Tan, A. K. & Chuang, I. L. Grand unification of quantum algorithms. *PRX quantum* **2**, 040203 (2021).
[43] Garratt, S. & Choi, S. Quantum algorithm to prepare quasi-stationary states (2024). *arXiv preprint arXiv:2407.07893* .
[44] Srakaew, K. *et al.* A subwavelength atomic array switched by a single rydberg atom. *Nature Physics* **19**, 714–719 (2023).
[45] Bekenstein, R. *et al.* Quantum metasurfaces with atom arrays. *Nature Physics* **16**, 676–681 (2020).
[46] Satzinger, K. J. *et al.* Realizing topologically ordered states on a quantum processor. *Science* **374**, 1237–1241 (2021).
[47] Morvan, A. *et al.* Formation of robust bound states of interacting microwave photons. *Nature* **612**, 240–245 (2022).
[48] Roberts, G. *et al.* Manybody interferometry of quantum fluids. *Science Advances* **10**, eado1069 (2024).
[49] Ma, R. *et al.* A dissipatively stabilized Mott insulator of photons. *Nature* **566**, 51–57 (2019).
[50] Saxberg, B. *et al.* Disorder-assisted assembly of strongly correlated fluids of light. *Nature* **616**, 435–441 (2022).
[51] Roberts, G. *et al.* Manybody interferometry of quantum fluids. *Science Advances* **10**, eado1069 (2024).
[52] Koch, J. *et al.* Charge-insensitive qubit design derived from the cooper pair box. *Phys. Rev. A* **76**, 042319 (2007).
[53] Vrajitoarea, A., Roberts, G., Hazzard, K. R., Simon, J. & Schuster, D. I. Sound waves in quantum fluids of light. *(in preparation)* .
[54] Paredes, B. *et al.* Tonks–Girardeau gas of ultracold atoms in an optical lattice. *Nature* **429**, 277–281 (2004).
[55] Léonard, J. *et al.* Realization of a fractional quantum hall state with ultracold atoms. *Nature* 1–5 (2023).
[56] Cazalilla, M. A., Citro, R., Giamarchi, T., Orignac, E. & Rigol, M. One dimensional bosons: From condensed matter systems to ultracold gases. *Reviews of Modern Physics* **83**, 1405–1466 (2011).
[57] Monz, T. *et al.* 14-qubit entanglement: Creation and coherence. *Phys. Rev. Lett.* **106**, 130506 (2011).
[58] Escher, B. M., de Matos Filho, R. L. & Davidovich, L. General framework for estimating the ultimate precision limit in noisy quantum-enhanced metrology. *Nature Physics* **7**, 406–411 (2011).
[59] Bohmann, M., Sperling, J. & Vogel, W. Entanglement and phase properties of noisy noon states. *Phys. Rev. A* **91**, 042332 (2015).
[60] Bylander, J. *et al.* Noise spectroscopy through dynamical decoupling with a superconducting flux qubit. *Nature Physics* **7**, 565–570 (2011).

[61] Zeng, Z. *et al.* Adiabatic echo protocols for robust quantum many-body state preparation. *arXiv preprint arXiv:2506.12138* (2025).
[62] Hahn, E. L. Spin echoes. *Phys. Rev.* **80**, 580–594 (1950).
[63] Hauke, P., Heyl, M., Tagliacozzo, L. & Zoller, P. Measuring multipartite entanglement through dynamic susceptibilities. *Nature Physics* **12**, 778–782 (2016).
[64] Vorobyov, V. *et al.* Quantum fourier transform for nanoscale quantum sensing. *npj Quantum Information* **7**, 124 (2021).
[65] Motlagh, D. & Wiebe, N. Generalized quantum signal processing. *PRX Quantum* **5**, 020368 (2024).
[66] Pichler, H., Zhu, G., Seif, A., Zoller, P. & Hafezi, M. Measurement protocol for the entanglement spectrum of cold atoms. *Physical Review X* **6**, 041033 (2016).

X. METHODS

Device Fabrication

The superconducting circuit was fabricated on a 10×20 mm C-plane sapphire chip. Prior to deposition, the 450 μm thick sapphire wafer was subjected to a thorough cleaning procedure, which included annealing at 1500°C for 2 hours, sequential solvent cleaning, and etching in heated 80°C Nano-Strip and 40°C sulfuric acid to ensure a pristine surface. The device features were patterned in two lithography steps. First, optical lithography was employed to define the large-scale components, including the wiring and ground plane, in a 200 nm thick tantalum (Ta) base layer. This Ta film was deposited at 800°C and then patterned using a direct pattern writer (Heidelberg MLA 150) followed by wet etching with hydrofluoric acid (HF).The second step involved electron-beam (e-beam) lithography to define the critical, small-scale features: the aluminum (Al) Josephson junctions (JJs) and superconducting quantum interference device (SQUID) loops. A MMA-PMMA bilayer resist was exposed using a Raith EBPG5000 Plus E-Beam Writer. The Al/AlO_x/Al Manhattan-style JJs were formed via a shadow evaporation technique in an angled e-beam evaporator (Plassys MEB550). Before the initial Al deposition, Argon (Ar) ion milling was performed on the exposed Ta features to remove any native Ta oxide, guaranteeing an improved ohmic contact between the Ta base layer and the superconducting Al layers. The first 60 nm Al layer was evaporated at 0.1 nm/s at an angle of 30° relative to the substrate normal. The oxidation barrier was formed by exposing the first Al layer to O_2 gas for 24 minutes at a pressure of 50 mBar. The final 150 nm Al layer was evaporated at the same rate and 30° angle, but with the substrate rotated 90° in-plane relative to the first evaporation, completing the overlapped junction structure.

Device Parameters

The Bose-Hubbard Hamiltonian for microwave photons is realized in a one-dimensional chain of capacitively coupled transmon qubits. The device is engineered to achieve a nearest-neighbor photon tunneling energy of $J/2\pi \approx 9$ MHz via capacitive coupling. The intrinsic transmon nonlinearity is used to provide a strong photon-photon interaction energy of $U/2\pi \approx 240$ MHz. These parameters were optimized through finite element simulations (Ansys HFSS) and experimental iteration. Each qubit is connected to a dedicated readout resonator and Purcell filter for state detection. A table of system parameters and further device details are available in section SI A. The optimal qubit lattice frequency was periodically adjusted between $4.8 - 5.3$ GHz throughout the experiment to mitigate the influence of two-level system (TLSs) defects. Coherence times exhibited temporal variation, with typical averages of $T_1 \approx 45$ μs and $T_2^* \approx 1.5$ μs. Operating all qubits at resonance provides an effective flux sweet-spot due to avoided crossings, which is expected to enhance T_2 during the disorder-free lattice evolution.

Microwave Wiring

The superconducting chip is mounted and heavily wire-bonded to a multilayer copper PCB. Dense wire-bonding around the device ensures a continuous ground plane and suppresses spurious slotline modes. The PCB assembly is secured within an oxygen-free high conductivity (OFHC) copper mount. This packaged sample is then mounted to the mixing chamber plate of a dilution refrigerator operating at a base temperature of approximately $8 - 9$ mK. To prevent external noise and radiation from interfering with the device, the sample is enclosed in extensive shielding, typically comprising nested layers of copper, superconducting lead, and MuMetal. Control microwave signals are routed from the room-temperature measurement setup through microwave coaxial cables. DC signals used for flux biasing the transmon SQUIDs are routed through twisted pair lines connected to individual on-chip lines inductively coupled to each SQUID. A separate solenoid of coiled niobium-titanium (NbTi) wire, mounted to the sample package, provides a global magnetic field used for tuning the qubits close to the desired frequency configuration, with minimal heating compared to driving the individual flux bias lines. Superconducting NbTi coaxial lines carry the multiplexed output signal of the readout resonators from the device feedline to the room-temperature homodyne measurement setup, going through a low-noise high-electron-mobility transistor (HEMT) amplifier mounted to the 4 K plate of the dilution refrigerator. See the supplemental information of our previous work [50] for further details on the cryogenic and room-temperature wiring.

Flux Control and Crosstalk

We control in real-time the frequencies of the transmon qubits by biasing their respective SQUID loops with magnetic fields supplied with currents sent through the inductively coupled bias lines. The frequency range $\omega_{01}/2\pi \approx (4-6)$ GHz allows us to tune the lattice potential between different ordered and disordered configuration (see SI A). The mutual inductive coupling with other SQUID loops creates non-negligible cross-talk, which we address by measuring and inverting a calibrated cross-talk matrix for DC and RF flux signals. Additional details are available in section SI C

Readout

On-site microscopy is done by sending microwave tones through the device feedline to probe the response of individual readout resonators dispersively coupled to each transmon qubit. Assuming the qubit populations are restricted in the $(|0\rangle, |1\rangle, |2\rangle)$ manifold, we probe the readout resonators at two separate frequencies to maximally distinguish the states $|0\rangle$ from $|1\rangle, |2\rangle$, and $|1\rangle$ from $|0\rangle, |2\rangle$. Our single-shot readout fidelities are in the range $85-95\%$. The non-negligible binning errors are corrected with a calibrated confusion matrix.

A. Data Availability

The experimental data presented in this manuscript are available from the corresponding author upon request, due to the proprietary file formats employed in the data collection process.

B. Code Availability

The source code for simulations throughout are available from the corresponding author upon request.

C. Additional Information

Correspondence and requests for materials should be addressed to A.V. (andrei.v@nyu.edu) and D.S. (dschus@stanford.edu). Supplementary information is available for this paper.

Supplementary Files

This is a list of supplementary files associated with this preprint. Click to download.

- Supplementalinformation.pdf